


 Cite this: *RSC Adv.*, 2021, **11**, 25658

# 3D printed MOF-based mixed matrix thin-film composite membranes†

 Sameh K. Elsaidi,<sup>id</sup>\*<sup>ab</sup> Mayur Ostwal,<sup>cd</sup> Lingxiang Zhu,<sup>id</sup><sup>ae</sup> Ali Sekizkardes,<sup>id</sup><sup>ae</sup> Mona H. Mohamed,<sup>fg</sup> Michael Gipple,<sup>ah</sup> Jeffrey R. McCutcheon<sup>\*cd</sup> and David Hopkinson<sup>a</sup>

MOF-based mixed-matrix membranes (MMMs) have attracted considerable attention due to their tremendous separation performance and facile processability. In large-scale applications such as CO<sub>2</sub> separation from flue gas, it is necessary to have high gas permeance, which can be achieved using thin membranes. However, there are only a handful of MOF MMMs that are fabricated in the form of thin-film composite (TFC) membranes. We propose herein the fabrication of robust thin-film composite mixed-matrix membranes (TFC MMMs) using a three dimensional (3D) printing technique with a thickness of 2–3 μm. We systematically studied the effect of casting concentration and number of electrospray cycles on membrane thickness and CO<sub>2</sub> separation performance. Using a low concentration of polymer of intrinsic microporosity (PIM-1) or PIM-1/HKUST-1 solution (0.1 wt%) leads to TFC membranes with a thickness of less than 500 nm, but the fabricated membranes showed poor CO<sub>2</sub>/N<sub>2</sub> selectivity, which could be attributed to microscopic defects. To avoid these microscale defects, we increased the concentration of the casting solution to 0.5 wt% resulting in TFC MMMs with a thickness of 2–3 μm which showed three times higher CO<sub>2</sub> permeance than the neat PIM-1 membrane. These membranes represent the first examples of 3D printed TFC MMMs using the electrospray printing technique.

 Received 21st April 2021  
 Accepted 17th June 2021

DOI: 10.1039/d1ra03124d

[rsc.li/rsc-advances](http://rsc.li/rsc-advances)

## 1. Introduction

Mixed-matrix membranes (MMMs) have emerged as a promising technology for gas separation applications.<sup>1–7</sup> They combine the advantages of polymeric membranes, including robustness and ease of fabrication, and the inorganic materials for their superb separation performance. This improved performance can be more pronounced if thin-film composite (TFC) membranes are used because membrane thinning can allow for high gas flux and gas permeation without compromising selectivity.<sup>8–10</sup> Metal-organic frameworks (MOFs) have

gained significant attention as filler particles in MMMs due to their high degree of modularity, permanent porosity, tunable pore size, and multifarious functionalities.<sup>11–18</sup> However, it is a challenge to fabricate continuous and defect-free TFC MMMs. TFC membranes can be fabricated *via* various approaches, such as interfacial polymerization, dip coating, spin coating, slot-die coating, knife coating, and bar coating.<sup>19–21</sup> However, these methods have some challenges that are not suitable for MOFs, such as using aggressive chemicals, complexity and limitations in processing.<sup>22–25</sup> Three-dimension (3D) printing or additive manufacture (AM) has found its applications in various areas, such as medicine, constructions, art, automotive, aerospace, and engineering.<sup>26,27</sup> However, the use of 3D printing for the fabrication of the separation membranes is relatively new.<sup>28</sup> 3D printing techniques could provide more control towards the design, shape, thickness, and roughness of the separation membrane, which cannot be achieved using conventional fabrication techniques.<sup>28,29</sup> Besides, 3D membrane printing can deliver numerous benefits that are highly desirable for the manufacturing, commercialization, and practicality of MMMs, such as speed, cost, precision, consistency, and quality. Recent research has shown a tremendous capacity for 3D printing to control membrane smoothness and thickness, exemplified by the 3D printed polyamide membrane reaching a thickness as low as 15 nm.<sup>30</sup>

On the other hand, 3D printing of mixed-matrix membranes (MMMs) is generally unexplored. A recent report demonstrated

<sup>a</sup>DOE National Energy Technology Laboratory (NETL), Pittsburgh, PA, 15236, USA. E-mail: samehelsaidi@mail.usf.edu

<sup>b</sup>Oak Ridge Institute for Science and Education, Pittsburgh, PA, 15236, USA

<sup>c</sup>Connecticut Center for Applied Separations Technology, University of Connecticut, Storrs, CT, USA. E-mail: jeffrey.mccutcheon@uconn.edu

<sup>d</sup>Department of Chemical & Biomolecular Engineering, Center for Environmental Sciences and Engineering, University of Connecticut, Storrs, CT, USA

<sup>e</sup>Leidos Research Support Team, 626 Cochran Mill Road, P.O. Box 10940, Pittsburgh, PA, 15236, USA

<sup>f</sup>Chemistry Department, Faculty of Science, Alexandria University, P.O. Box 426, Ibrahimia, Alexandria, 21321, Egypt

<sup>g</sup>Department of Chemistry, University of Pittsburgh, 219 Parkman Avenue, Pittsburgh, PA, USA

<sup>h</sup>Deltha, New Orleans, LA, 70114, USA

† Electronic supplementary information (ESI) available. See DOI: 10.1039/d1ra03124d



the fabrication of mixed-matrix films (MMFs) using the 3D printing technique. The MMFs are fabricated as a single layer with different grid patterns using selective laser sintering for water purification applications.<sup>31</sup> As a part of our efforts to control and improve the MMM fabrication, we developed the first examples of 3D printed TFC MMMs consisting of HKUST-1 as filler and PIM-1 matrix using the electro-spray printing technique. This could be a breakthrough for MOF-based MMM scale-up and commercialization, which can only be realized using nanoscale MOFs to produce thin selective layers.

Fenn *et al.* used the electro-spray printing technique for mass spectrometry of large polar biomolecules.<sup>32</sup> Others used the same technique to make thin films, nanoparticles, or patterns.<sup>32–36</sup> We recently used the same approach to deposit individual monomers onto a substrate, subsequently polymerizing on the surface to create membranes for reverse osmosis.<sup>30</sup>

## 2. Experimental

### 2.1 Synthesis

**2.1.1 Synthesis of HKUST-1 nanoparticles.** HKUST-1 nanoparticles were synthesized according to modified literature procedures.<sup>37</sup>

HKUST-1 synthesis was performed using a direct mixing procedure using acetic acid as modulator. A 100 ml ethanolic solution of 1 mmol trimesic acid was mixed directly with a 100 ml solution of 2 mmol copper acetate dissolved in 90 ml water and 10 ml of acetic acid. An immediate sky blue color of HKUST-1 nanoparticles was formed and the suspended powder was centrifuged immediately to avoid crystal growth. HKUST-1 nanoparticles were thoroughly solvent-exchanged with ethanol, acetone then methanol to remove unreacted starting materials and acetic acid.

**2.1.2 Synthesis of PIM-1.** PIM-1 was synthesized by modification of the experimental method developed by Budd *et al.*<sup>38</sup> 3,3,3',3'-tetramethyl-1,1'-spirobisindane-5,5',6,6'-tetrol (27.6 mmol, 9.14 g) and 2,3,5,6-tetra-fluorophthalonitrile (27.6 mmol, 5.3 g) were dissolved in anhydrous dimethylformamide (DMF) (250 ml). Potassium carbonate (K<sub>2</sub>CO<sub>3</sub>) was added in the solution and the reaction was stirred at 58 °C for 40 hours. Water (400 ml) was added after cooling the reaction mixture and the product was separated by filtration. Further purification was performed by reprecipitation from the CHCl<sub>3</sub> solution with MeOH and a bright yellow solid product was produced (11.4 g, yield 92%) after thermal activation at 120 °C.

#### 2.1.3 Membrane fabrication

**2.1.3.1 Preparation of 2 wt% PIM-1 solution.** A 2 g of PIM-1 was added to 98 g of chloroform. The solution was then sonicated until the polymer is completely soluble.

**2.1.3.2 Preparation of 2 wt% PIM-1/HKUST-1 solution.** In a glove box, 300 mg of activated MOF nanoparticles is added to the 1.7 g of PIM-1 in 98 g of chloroform and sonicated for several hours until all the MOF particles get suspended.

The 0.1 wt% and 0.5 wt% solutions of PIM-1 and PIM-1/HKUST-1 were prepared by dilution of the 2 wt% solutions with chloroform.

**2.1.3.3 Membrane fabrication (electrospray deposition of PIM-1/HKUST-1).** The membranes were fabricated following the 3D

printing (electrospray) procedure reported in literature.<sup>30</sup> The schematic for the electro-spray system utilized is shown in Fig. S1.† A stainless-steel needle was connected to a high voltage DC power source (Gamma High Voltage Research, Ormond Beach, FL) which can generate up to 30 kV. A 12" diameter rotating drum was grounded to generate potential difference between the drum and the needle tip. The needle was suspended from an L-shaped arm attached to a stage. ~5 cm distance was kept between the needle tip and the rotating drum. The stage was mounted on a screw slider moves horizontally (across the length of the rotating drum) using a stepper motor that is controlled by a motor controller (Velmex, Bloomfield, NY).

To print the membrane on the support, the drum is first covered with a Aluminum foil and the PAN 400 support (~3" × 6") was then attached and wrapped around the foil-wrapped drum using tape. Part of the aluminum foil on the edges was left exposed. PIM-1 and HKUST-1 solution (0.1 or 0.5 wt%) was then fed to the needle using a syringe pump at a flowrate of 20 ml h<sup>-1</sup> using flexible tubing. Electro-spraying was initiated on the exposed (not covered with PAN 400 support) aluminum foil to allow the spray to stabilize. Stable spray refers to a cone-jet mode where the liquid is elongated into a long, fine jet of droplets which deposit onto the substrate surface. The applied voltage was around 6.8 kV. Once the spray was stabilized, the Velmex controller was activated which was programmed to begin the movement of the needle stage over 12 cm horizontally as the drum turned (at 15 rpm). As the drum rotates, the PIM-1 and HKUST-1 solution gets deposited on the PAN support. When the needle traverses the entire PAN 400 support once, that was considered "one scan" or "one cycle". For multiple scans, the stage would come back to the original position at a speed of 5 cm s<sup>-1</sup> and start the next scan. The number of scans were varied from 2–5. After the desired number of scans was done, the sample was removed, and the delivery line was cleaned with chloroform and dried with air.

## 3. Characterization

### 3.1 Powder X-ray diffraction

XRD pattern for the crystalline powder of MOF nanoparticles were recorded on a Panalytical X'Pert Pro MPD X-ray Diffractometer using Cu K $\alpha$  radiation ( $\lambda = 1.54 \text{ \AA}$  at 45 kV and 40 mA) at room temperature. Diffraction data were collected at a scan speed of 0.1° min<sup>-1</sup>, step size of 0.03° and a 2 $\theta$  range of 5–40°.

### 3.2 Ultraviolet-visible spectroscopy (UV-VIS)

The UV-VIS of the MOF/polymer dispersed solutions in chloroform were collected on an Agilent 8453 UV-VIS spectrometer.

### 3.3 Gas sorption measurements

Adsorption measurements were conducted on the crystalline powder of HKUST-1 using a Micromeritics 3Flex surface area and gas analyzer instrument within the  $P/P_0$  range of 0–1.0.



### 3.4 Scanning electron microscope (SEM)

SEM measurements were performed to determine the quality of the fabricated membranes. The samples were prepared by fracturing the membranes in liquid nitrogen and subsequent sputter coating of palladium using a SPI Module Sputter Coater. SEM images were collected using a FEI Company Quanta 600 field-emission scanning electron microscope. SEM was used with a beam energy of 10 kV and a working distance of  $\sim 10$  mm in secondary electron mode to examine the morphology of the membranes.

### 3.5 Gas permeation measurements

Pure-gas permeances of TFC membranes were measured in a customized constant-pressure variable volume system. The membrane sample was first masked by a 50  $\mu\text{m}$  thick copper shim using epoxy to seal the rim of the mask before being sealed inside a stainless-steel permeation membrane cell. The active membrane area for gas permeation was about 1  $\text{cm}^2$ . Pure  $\text{CO}_2$  or  $\text{N}_2$  was introduced to the upstream side of the membrane at 1 barg while keeping the permeate side at atmospheric pressure. The *trans*-membrane steady-state flux was measured using a soap bubble flow meter ( $< 0.1 \text{ cm}^3 \text{ min}^{-1}$ ) and a digital mass flow meter ( $0.1\text{--}20 \text{ cm}^3 \text{ min}^{-1}$ ) at the room temperature of 22  $^\circ\text{C}$ . To exclude the interference of physical aging effect, all the membrane samples were pretreated with 24 h methanol soaking, followed by a vacuum drying at 40  $^\circ\text{C}$  for 3 hours prior to the measurement.

## 4. Results and discussion

The choice of the HKUST-1 as a filler and PIM-1 as a matrix was based on our previous study,<sup>39</sup> which revealed their chemical compatibility and their separation performance. The free nitrile

functional groups in the PIM-1 backbone can strongly interact with the unsaturated Cu metal centers of HKUST-1. This chemical interaction is important for optimizing the MOF-polymer interfacial compatibility. Fig. S2<sup>†</sup> shows the ultraviolet-visible spectroscopy (UV-VIS) of a PIM-1/HKUST-1 nanoparticles solution in chloroform. A peak shift to higher energy was observed from 700 nm in HKUST-1 to 580 nm in the PIM-1/HKUST-1 mixture. This could indicate the variation in the Cu electronic environment in HKUST-1 upon the interaction with cyano groups from PIM-1 backbone.

X-ray photoelectron spectroscopy (XPS) was used as an evidence for the HKUST-1/PIM-1 interaction.<sup>39</sup> The XPS  $\text{N}_{1s}$  spectra of PIM-1 revealed two equally intense components to the  $\text{N}_{1s}$  spectrum at 397.7 eV and 399.7 eV from the  $\text{C}\equiv\text{N}$  functionality of PIM-1. Upon mixing HKUST-1 with PIM-1, the unsaturated Cu centers on the surface of the HKUST-1 can coordinate with the  $\text{C}\equiv\text{N}$  of PIM-1 resulted in a shift of the 399.7 eV component of the  $\text{N}_{1s}$  spectrum to 397.7 eV and an increase in the relative intensity of the other component.<sup>39</sup>

The formation of small MOF nanoparticles is highly desirable for the uniform distribution of polymer/MOF solution on the substrate. Therefore, we were able to synthesize HKUST-1 nanoparticles in small sizes of  $\sim 30\text{--}50$  nm (Fig. S3<sup>†</sup>), as revealed by scanning electron microscopy (SEM). The powder X-ray diffraction (PXRD) showed the high crystallinity of the HKUST-1 nanoparticles (Fig. S4<sup>†</sup>), and the  $\text{N}_2$  adsorption isotherm at 77 K revealed the retention of high porosity (BET surface area = 1869  $\text{m}^2 \text{ g}^{-1}$ , Fig. S5<sup>†</sup>).

PIM-1/HKUST-1 mixture was deposited as nanoscale droplets using the electrospray technique forming TFC MMMs on a substrate surface. The electrospray system schematic (Fig. 1 and S1<sup>†</sup>) and detailed printing procedure are described in the ESL.<sup>†</sup> In this technique, the liquid containing the MOF/polymer mixture

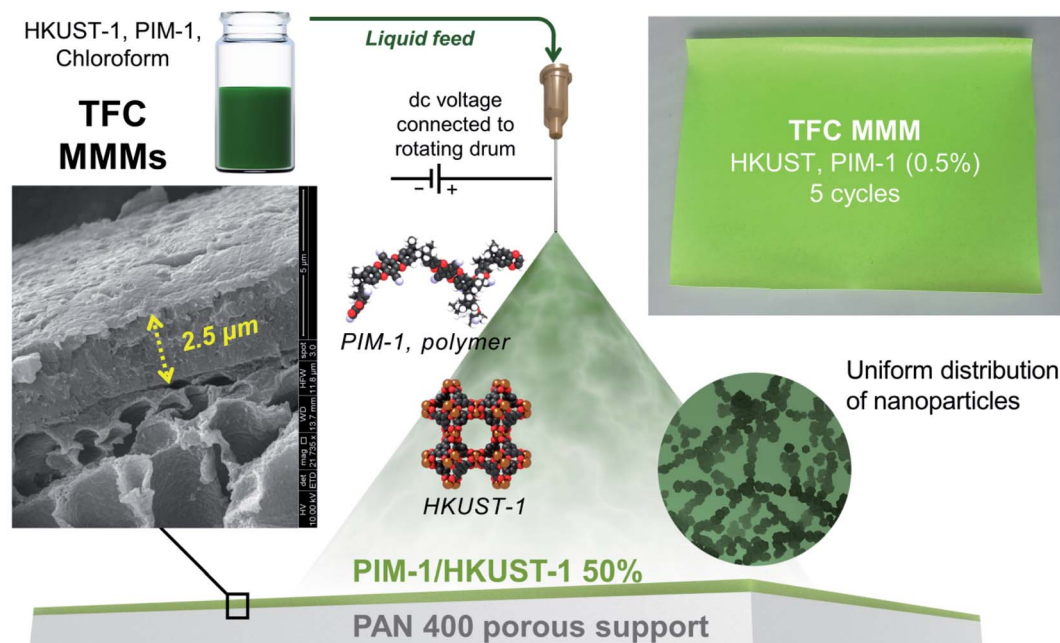


Fig. 1 Schematic demonstration of the electrospray 3D printing approach.



(PIM-1 and HKUST-1 in chloroform) is extruded from the needle in the presence of a strong electric field. This field forces the ejected droplets to spread well with diameters below 1  $\mu\text{m}$  (Fig. 1).

The solution droplet emerging from the needle is then sprayed and deposited on the substrate. The needle moves horizontally over and across the substrate attached on a rotating drum to form a uniform coating. The drum is grounded and connected to the needle through a high-voltage dc power supply that can produce up to 30 kV. A polyacrylonitrile (PAN) microporous membrane was used as a porous substrate due to its superior chemical stability among the commercial microporous membranes. The needle stage passes along the collector surface to

ensure coverage of the entire substrate. A single sweep over the surface is denoted as a single scan or cycle. The number of scans or cycles then controlled the thickness of the selective layer.

PXRD confirmed that the MOF structures retained their crystallinity after the membrane fabrication (Fig. S6 in ESI<sup>†</sup>). The peaks of the PAN support were observed in both the PIM-1 and PIM-1/HKUST-1 TFCs. The SEM revealed the successful fabrication of the TFC membranes (Fig. 2). The membrane thickness of the neat polymer or the TFC MMM-1 using a low concentration (0.1 wt%) of PIM-1 or PIM-1/HKUST-1 was around 400–500 nm. In comparison, the higher concentration solution (0.5 wt%) led to thicker PIM-1 and TFC MMM-2

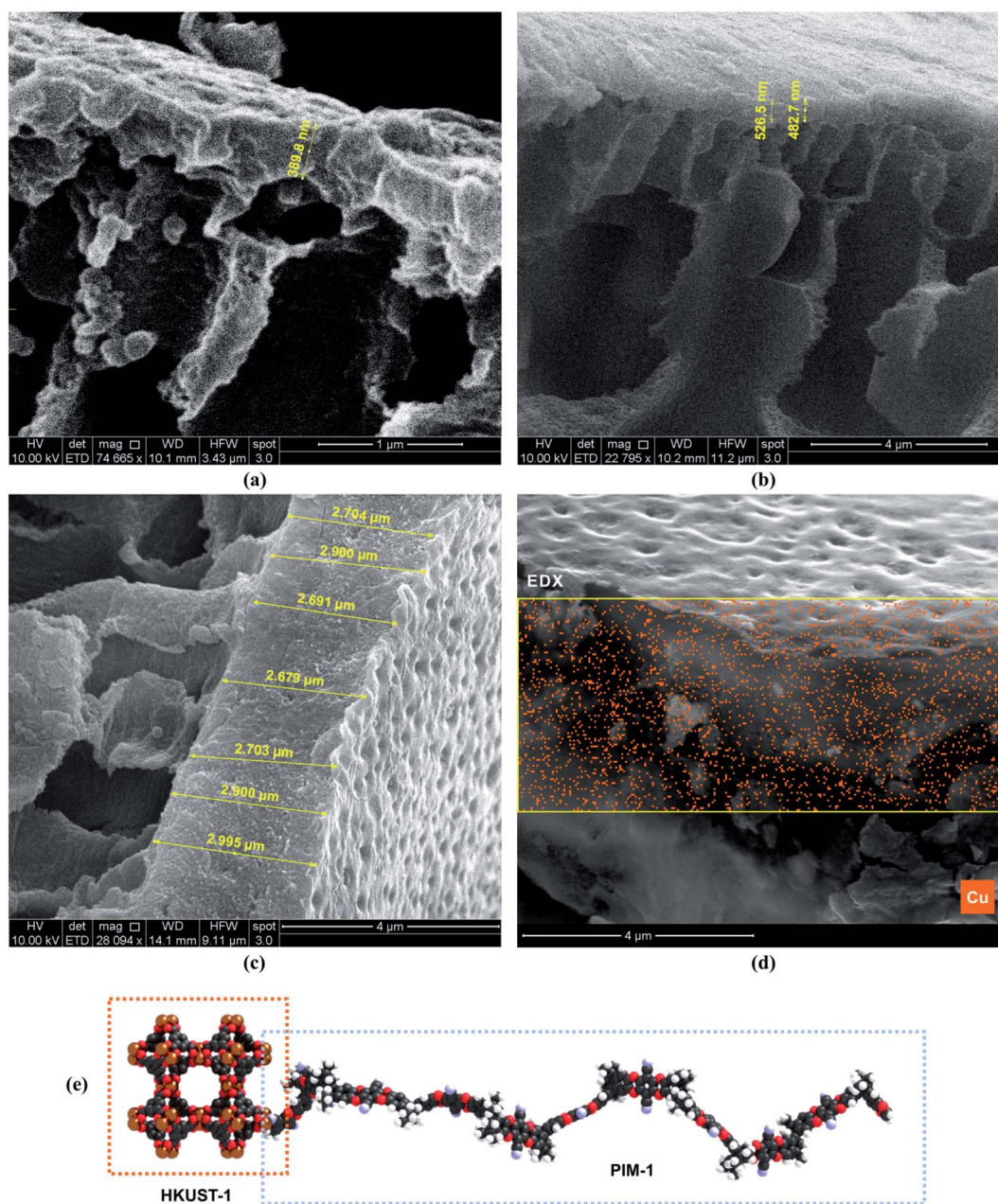


Fig. 2 SEM images of the fabricated TFC membranes (5 cycles). (a) 0.1 wt% PIM-1, (b) 0.1 wt% PIM-1/HKUST-1, (c) 0.5 wt% PIM-1/HKUST-1, (d) EDX analysis of 0.5 wt% PIM-1/HKUST-1, and (e) representation of the chemical interaction between the open metal site of the HKUST-1 and the cyano group of PIM-1. The scale bar is shown below each image. The thickness of the membrane is measured in yellow.



**Table 1** Summary of the gas transport properties at 22 °C of the 3D printed TFC membranes (LC for low concentration and HC for high concentration)

Membrane	Thickness		CO <sub>2</sub> permeance (GPU)	CO <sub>2</sub> /N <sub>2</sub> selectivity
	(μm)	wt%		
PIM-1 (LC)	0.39	0.1	147	2.6
TFC MMM-1	0.5	0.1	305	2
PIM-1 (HC)	2.75	0.5	159	12
TFC MMM-2	2.75	0.5	696	6.4

selective layers with a thickness of 2.5–3 μm. As shown in Fig. S7 in ESI,† PIM-1 TFC prepared by low concentration of PIM-1 (0.1 wt%) showed microscopic defects that are shown only in the surface of the membrane. Therefore, we decided to increase the concentration of the casting solution (PIM-1 and PIM-1/HKUST-1) from 0.1 wt% to 0.5 wt%. SEM cross-sectional and surface images of the fabricated TFC membranes at high concentration of 0.5 wt% did not reveal any noticeable defects (Fig. S8–S11†). The energy-dispersive X-ray spectroscopy (EDX) revealed that MOF nanoparticles (Cu in HKUST-1) were distributed uniformly throughout the membrane cross-section with no visible defects or large-scale phase separation (Fig. 2d).

As a proof-of-concept demonstration for gas separation applications, we tested these membranes for CO<sub>2</sub> separation from flue gas. The gas permeation data revealed that the membranes prepared using a low concentration PIM-1 or PIM-1/HKUST-1 mixture (0.1 wt%) with the membrane thickness below 500 nm showed poor CO<sub>2</sub>/N<sub>2</sub> selectivity, which might be attributed to small defects or imperfections in the fabricated membranes.

After increasing the concentration of the PIM-1 to 0.5 wt%, the membrane selectivity of the neat polymer is dramatically enhanced from 2.6 to 12 for 5 coating cycles. The same behavior was observed in the TFC MMMs by increasing the PIM-1/HKUST-1 concentration to 0.5 wt% and membrane thickness to 2–3 μm, the CO<sub>2</sub>/N<sub>2</sub> selectivity is increased from 2 to 6.4 (Tables 1 and S1;† Fig. 3). Although the CO<sub>2</sub>/N<sub>2</sub> selectivity of the HKUST-1/PIM-1 TFC MMM is decreased compared to the neat

polymer, the TFC MMM B#2 showed four times higher CO<sub>2</sub> permeance than the neat PIM-1 B#1 membrane. This is a typical trade-off when highly porous filler particles are added to a polymer matrix.

We also examined the impact of the number of coverage cycles on membrane performance. Using a high concentration of PIM-1, the TFC membrane fabricated using two coverage cycles (PIM-1 B#1) showed comparable permeability and selectivity to the one with five cycles (PIM-1 B#2), which indicates a full coverage of the substrate and formation of membranes without significant defects in both cases. Also, as would be expected, the membrane permeance scales with inverse proportion to selective layer thickness, with more cycles leading to greater thickness.

## 5. Conclusions

In summary, we successfully fabricated MOF-based TFC-MMMs by incorporating HKUST-1 nanoparticles into a PIM-1 matrix *via* the 3D electrospay printing technique. The membrane thickness was reduced to maximize the gas permeance while still ensuring that the fabricated membranes are defect-free and sufficiently robust. The thinner membranes (<500 nm) showed a much lower CO<sub>2</sub>/N<sub>2</sub> selectivity, which might be attributed to microscopic defects. However, by increasing the concentration of the membrane compositions to 0.5 wt%, we fabricate 2–3 μm continuous TFC membranes thanks to the high control of the electrospay 3D printing technique. The 2–3 μm thick TFC membranes showed a drastic improvement in CO<sub>2</sub>/N<sub>2</sub> selectivity compared to the thinner membranes. Although TFC MMMs had reduced CO<sub>2</sub>/N<sub>2</sub> selectivity, the MMM showed much higher CO<sub>2</sub> permeance than the neat polymer.

## Conflicts of interest

There are no conflicts to declare.

## Acknowledgements

This technical report was performed in support of the National Energy Technology Laboratory's ongoing research in CO<sub>2</sub> capture under the Carbon Capture field work proposal. This project was funded by the U.S. Department of Energy, National Energy Technology Laboratory, an agency of the United States Government, in part through a support contract with Leidos. Funding was also provided through the Connecticut Center for Applied Separations Technology which is supported by the Connecticut Department of Economic and Community Development. Additional funding and support came from NSF CMMI #2001624. Neither the United States Government nor any agency thereof, nor any of their employees, nor Leidos, nor any of their employees, makes any warranty, expressed or implied, or assumes any legal liability or responsibility for the accuracy, completeness, or usefulness of any information, apparatus, product, or process disclosed, or represents that its use would not infringe privately owned rights. Reference herein to any specific commercial product, process, or service by trade name,

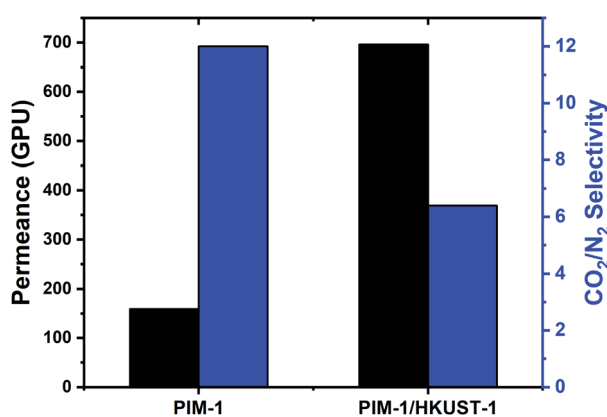


**Fig. 3** The gas transport properties of the PIM-1/HKUST-1 TFC MMM compared to neat PIM-1 TFC membrane. The CO<sub>2</sub> permeance in GPU (gray) and CO<sub>2</sub>/N<sub>2</sub> selectivity (blue).



trademark, manufacturer, or otherwise, does not necessarily constitute or imply its endorsement, recommendation, or favoring by the United States Government or any agency thereof. The views and opinions of authors expressed herein do not necessarily state or reflect those of the United States Government or any agency thereof.

## References

- 1 M. Aroon, A. Ismail, T. Matsuura and M. Montazer-Rahmati, *Sep. Purif. Technol.*, 2010, **75**, 229–242.
- 2 B. Ghalei, K. Sakurai, Y. Kinoshita, K. Wakimoto, A. P. Isfahani, Q. Song, K. Doitomi, S. Furukawa, H. Hirao, H. Kusuda, S. Kitagawa and E. Sivaniah, *Nat. Energy*, 2017, **2**, 17086.
- 3 G. Liu, V. Chernikova, Y. Liu, K. Zhang, Y. Belmabkhout, O. Shekhah, C. Zhang, S. Yi, M. Eddaoudi and W. J. Koros, *Nat. Mater.*, 2018, **17**, 283–289.
- 4 M. S. Denny Jr, J. C. Moreton, L. Benz and S. M. Cohen, *Nat. Rev. Mater.*, 2016, **1**, 16078.
- 5 T. Rodenas, I. Luz, G. Prieto, B. Seoane, H. Miro, A. Corma, F. Kapteijn, F. X. Llabrés i Xamena and J. Gascon, *Nat. Mater.*, 2014, **14**, 48.
- 6 Y. Cheng, Y. Ying, S. Japip, S.-D. Jiang, T.-S. Chung, S. Zhang and D. Zhao, *Adv. Mater.*, 2018, **30**, 1802401.
- 7 J. Dechnik, J. Gascon, C. J. Doonan, C. Janiak and C. J. Sumbly, *Angew. Chem., Int. Ed.*, 2017, **56**, 9292–9310.
- 8 W. Lau, A. Ismail, N. Misdan and M. Kassim, *Desalination*, 2012, **287**, 190–199.
- 9 Q. Fu, J. Kim, P. A. Gurr, J. M. P. Scofield, S. E. Kentish and G. G. Qiao, *Energy Environ. Sci.*, 2016, **9**, 434–440.
- 10 C. Ma, M. Wang, Z. Wang, M. Gao and J. Wang, *J. CO<sub>2</sub> Util.*, 2020, **42**, 101296.
- 11 H. Furukawa, K. E. Cordova, M. O’Keeffe and O. M. Yaghi, *Science*, 2013, **341**, 1230444.
- 12 J.-R. Li, R. J. Kuppler and H.-C. Zhou, *Chem. Soc. Rev.*, 2009, **38**, 1477–1504.
- 13 X. Zhao, Y. Wang, D.-S. Li, X. Bu and P. Feng, *Adv. Mater.*, 2018, **30**, 1705189.
- 14 H. Furukawa, N. Ko, Y. B. Go, N. Aratani, S. B. Choi, E. Choi, A. Ö. Yazaydin, R. Q. Snurr, M. O’Keeffe, J. Kim and O. M. Yaghi, *Science*, 2010, **329**, 424–428.
- 15 H.-C. Zhou, J. R. Long and O. M. Yaghi, *Chem. Rev.*, 2012, **112**, 673–674.
- 16 H. Deng, C. J. Doonan, H. Furukawa, R. B. Ferreira, J. Towne, C. B. Knobler, B. Wang and O. M. Yaghi, *Science*, 2010, **327**, 846–850.
- 17 D. Zhao, D. J. Timmons, D. Yuan and H.-C. Zhou, *Acc. Chem. Res.*, 2011, **44**, 123–133.
- 18 S. K. Elsaidi, M. H. Mohamed, D. Banerjee and P. K. Thallapally, *Coord. Chem. Rev.*, 2018, **358**, 125–152.
- 19 S. Yu, S. Li, Y. Liu, S. Cui and X. Shen, *J. Membr. Sci.*, 2019, **573**, 425–438.
- 20 T. K. Goh, S. N. Guntari, C. J. Ochs, A. Blencowe, D. Mertz, L. A. Connal, G. K. Such, G. G. Qiao and F. Caruso, *Small*, 2011, **7**, 2863–2867.
- 21 B.-H. Jeong, E. M. Hoek, Y. Yan, A. Subramani, X. Huang, G. Hurwitz, A. K. Ghosh and A. Jawor, *J. Membr. Sci.*, 2007, **294**, 1–7.
- 22 A. Awad and I. H. Aljundi, *Energy*, 2018, **157**, 188–199.
- 23 V. Freger, J. Gilron and S. Belfer, *J. Membr. Sci.*, 2002, **209**, 283–292.
- 24 J. Ji, J. Dickson, R. Childs and B. McCarry, *Macromolecules*, 2000, **33**, 624–633.
- 25 J. Rühle and W. Knoll, *Journal of Macromolecular Science, Part C*, 2002, **42**, 91–138.
- 26 H. Lipson and M. Kurman, *Fabricated: The new world of 3D printing*, John Wiley & Sons, 2013.
- 27 F. Rengier, A. Mehndiratta, H. Von Tengge-Kobligk, C. M. Zechmann, R. Unterhinninghofen, H.-U. Kauczor and F. L. Giesel, *International journal of computer assisted radiology and surgery*, 2010, **5**, 335–341.
- 28 Z.-X. Low, Y. T. Chua, B. M. Ray, D. Mattia, I. S. Metcalfe and D. A. Patterson, *J. Membr. Sci.*, 2017, **523**, 596–613.
- 29 J.-Y. Lee, W. S. Tan, J. An, C. K. Chua, C. Y. Tang, A. G. Fane and T. H. Chong, *J. Membr. Sci.*, 2016, **499**, 480–490.
- 30 M. R. Chowdhury, J. Steffes, B. D. Huey and J. R. McCutcheon, *Science*, 2018, **361**, 682–686.
- 31 R. Li, S. Yuan, W. Zhang, H. Zheng, W. Zhu, B. Li, M. Zhou, A. Wing-Keung Law and K. Zhou, *ACS Appl. Mater. Interfaces*, 2019, **11**, 40564–40574.
- 32 J. B. Fenn, M. Mann, C. K. Meng, S. F. Wong and C. M. Whitehouse, *Science*, 1989, **246**, 64.
- 33 R. Saf, M. Goriup, T. Steindl, T. E. Hamedinger, D. Sandholzer and G. Hayn, *Nat. Mater.*, 2004, **3**, 323–329.
- 34 A. Jaworek and A. T. Sobczyk, *J. Electrostat.*, 2008, **66**, 197–219.
- 35 J.-U. Park, M. Hardy, S. J. Kang, K. Barton, K. Adair, D. Kishore Mukhopadhyay, C. Y. Lee, M. S. Strano, A. G. Alleyne and J. G. Georgiadis, *Nat. Mater.*, 2007, **6**, 782–789.
- 36 Y. K. Hwang, U. Jeong and E. C. Cho, *Langmuir*, 2008, **24**, 2446–2451.
- 37 S. K. Elsaidi, D. Ongari, W. Xu, M. H. Mohamed, M. Haranczyk and P. K. Thallapally, *Chem. – Eur. J.*, 2017, **23**, 10758–10762.
- 38 P. M. Budd, E. S. Elabas, B. S. Ghanem, S. Makhseed, N. B. McKeown, K. J. Msayib, C. E. Tattershall and D. Wang, *Adv. Mater.*, 2004, **16**, 456–459.
- 39 S. K. Elsaidi, S. Venna, A. K. Sekizkardes, J. A. Steckel, M. H. Mohamed, J. Baker, J. Baltrus and D. Hopkinson, *Cell Rep. Phys. Sci.*, 2020, **1**, 100113.

